Official journal of the JHL 2689-9620
www.light-am.com

Article Open Access

Rapid fabrication of reconfigurable helical microswimmers with environmentally adaptive locomotion

Rui Li[1], Yuan Tao[1], Jiawen Li[1*], Dongdong Jin[2], Chen Xin[1], Shengyun Ji[1], Chaowei Wang[1], Yachao Zhang[1], Yanlei Hu[1], Dong Wu[1], Li Zhang[2*] and Jiaru Chu[1]

Abstract

Artificial helical microswimmers with shape-morphing capacities and adaptive locomotion have great potential for precision medicine and noninvasive surgery. However, current reconfigurable helical microswimmers are hampered by their low-throughput fabrication and limited adaptive locomotion. Here, a rotary holographic processing strategy (a helical femtosecond laser beam) is proposed to produce stimuli-responsive helical microswimmers (<100 μm) rapidly (<1 s). This method allows for the easy one-step fabrication of various microswimmers with controllable sizes and diverse bioinspired morphologies, including spirulina-, Escherichia-, sperm-, and Trypanosoma-like shapes. Owing to their shape-morphing capability, the helical microswimmers undergo a dynamic transition between tumbling and corkscrewing motions under a constant rotating magnetic field. By exploiting adaptive locomotion, helical microswimmers can navigate complex terrain and achieve targeted drug delivery. Hence, these microswimmers hold considerable promise for diverse precision treatments and biomedical applications.

Keywords: Femtosecond laser beam, Rotary holographic processing, Helical microswimmer, Shape morphing, Adaptive locomotion

Introduction

Microorganisms can undergo adaptive shape morphing to optimize their locomotion mechanisms in the environment, which enables them to navigate complex barriers and improve survival[1–3]. Inspired by this autonomous behavior, artificial reconfigurable microrobots have been proposed to realize similar adaptation capabilities[4,5]. Such microrobots primarily rely on active materials (for example, stimuli-responsive hydrogels[6,7] and liquid crystal elastomer[8,9]) that can respond to external stimuli, including light[10,11], heat[12], and magnetic fields[13–15], and then generate controlled mechanical motion. Among the numerous stimuli-responsive microrobots, helical-like microswimmers are recognized as the most promising tools for in vivo biomedical applications because of their wireless, precise, and biologically harmless actuation under low-strength rotating magnetic fields[16,17]. Recently, various alternative schemes have been developed to fabricate shape-morphing helical microswimmers. For instance, self-folding heat-triggered helical microswimmers with

Correspondence: Jiawen Li (jwl@ustc.edu.cn) or Li Zhang (lizhang@mae.cuhk.edu.hk)
[1]CAS Key Laboratory of Mechanical Behavior and Design of Materials, Department of Precision Machinery and Precision Instrumentation, University of Science and Technology of China, Hefei 230026, China
[2]Department of Mechanical and Automation Engineering, The Chinese University of Hong Kong, Hong Kong 999077, China
These authors contributed equally: Rui Li, Yuan Tao

reconfigurable shapes and controllable motility have been realized using an origami-inspired ultraviolet (UV) curing process[18]. Moreover, helical microswimmers, capable of autonomous swimming by detecting the surrounding temperature changes, have been prepared using a buoyancy-assisted anisotropic gelation method[19]. However, although these schemes are usually suitable for producing morphable helical microswimmers of several millimeters, it can be challenging to use them for fabricating microswimmers at the microscale (<100 μm). In fact, many biological structural units are in the microscale range, including cells[20], capillaries[21], and wrinkles on biological surfaces[22]. Hence, there is an urgent demand for miniaturizing these morphable helical microswimmers to the microscale to deliver and treat single cells, access small and complex environments, and enhance the accuracy of targeted therapy.

Numerous methods, including self-scrolling[23,24], glancing angle deposition (GLAD)[25], and template-assisted deposition[26], have been developed to generate miniaturized helical microswimmers. However, these techniques are not applicable to active-material curing and morphable microswimmer fabrication. Femtosecond direct laser writing (fs-DLW), which is capable of multiple material printing, excellent 3D geometry design, and nanometer spatial resolution, has evolved into an outstanding method for fabricating reconfigurable helical microswimmers at the microscale[27,28]. These microswimmers can respond to multiple stimuli and find applications in drug delivery and release[29–32]. However, the following two challenges are worthy of further exploration. First, fs-DLW is a relatively inefficient fabrication strategy because of its point-by-point scanning[33], and it is difficult to produce large amounts of helical microswimmers in a short time using this strategy. For biological clinical trials in which thousands of microrobots are required, a highly efficient production of microrobots is essential. Second, current research on morphable helical microswimmers mainly focuses on their functionalities (for example, biodegradability[34,35] and biocompatibility[36]), and the adaptive locomotion of morphable microswimmers in complicated environments (for example, inside living organisms) requires further study. For instance, within the body, pH values vary among different tissues (for example, normal cells ~7.4, stomach ~1, intestine ~8.4, and tumor cells <7[37–39]) and there are numerous microchannels and obstacles. The ability of a microrobot to sense the external environment and perform adaptive locomotion across these networks is vital for in vivo targeted therapy. Consequently, there is high demand for a method to address these two difficulties.

In this study, we developed a rotary holographic processing strategy to fabricate pH-responsive helical hydrogel microswimmers (<100 μm) in a highly efficient manner (<1 s), which enables adaptive locomotion response to the surrounding environment. Based on this strategy, a 3D helical holographic femtosecond laser was generated to print helical microswimmers of different sizes (diameter and height) and morphologies (spirulina-, Escherichia-, sperm-, and Trypanosoma-like) in an easy and rapid one-step process. Compared with the traditional point-by-point scanning strategy, our method involved the use of a 3D-shaped laser to fabricate microswimmers one by one, which is approximately 100 times faster[34]. By altering the solution pH value, the helical microswimmers underwent tumbling motion in a contracted state and corkscrewing motion in an expanded state under a constant rotating magnetic field. This motion transition was due to the environmentally adaptive shape morphing of the microswimmers, rather than from adjusting the magnetic field. Moreover, the tumbling-to-corkscrewing transition enabled our microswimmers to traverse complex terrains (microwalls and microchannels) and realize targeted drug (DOXs) delivery. The proposed scheme opens an avenue for highly efficient production of shape-morphing helical microswimmers for accurate medical tasks.

Results and Discussion

Highly efficient fabrication of a stimuli-responsive microhelix based on the rotary holographic processing method

To solve the problem of the low-throughput fabrication of fs-DLW, holographic femtosecond laser processing has been reported as a robust way to modulate the laser beam into various 3D light fields, including multifocal spots[40], Bessel beams[41], and Airy beams[42]. This method is also suitable for rapidly fabricating microrobots. Fig. 1a illustrates the principle of rapid fabrication of a microhelix based on the rotary holographic processing method (Supplementary Movie S1). A rotary computer-generated hologram (RCGH) was developed by superimposing rotary local phase modulation (RLPM) on a computer-generated hologram (CGH), as shown in Fig. 1b. After being reflected from the spatial light modulator (SLM) loaded with the RCGH, a Gaussian femtosecond laser beam could be modulated into a specific 3D light field (Fig. 1c). The phase-type SLM used was a liquid-crystal-based light modulator with the gray scale value of 0–255, corresponding to a phase delay of 0–2π.

Initially, a spiral phase plate (SPP), axicon, and blazed grating (BG) were superimposed together to generate the CGH. The SPP and axicon can generate high-order Bessel

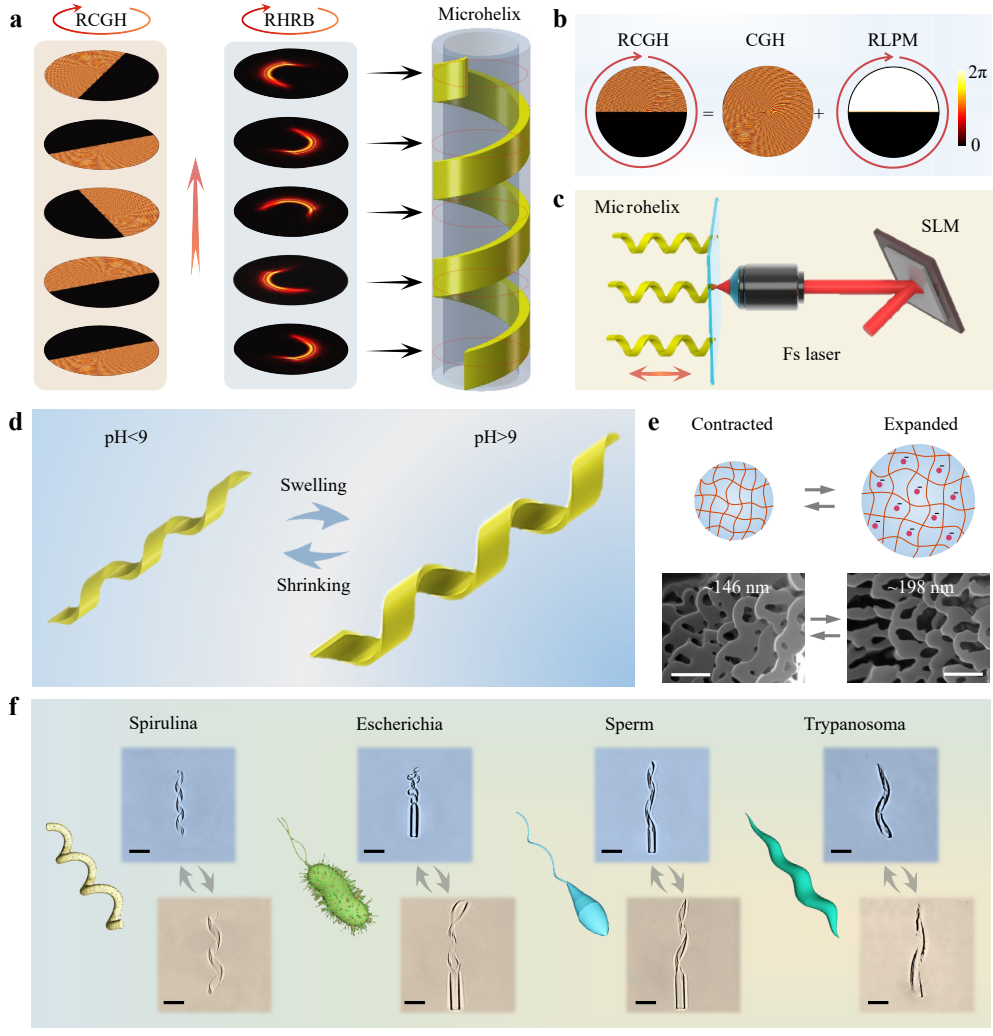

Fig. 1 Schematic illustration of highly efficient fabrication of a stimuli-responsive microhelix based on the rotary holographic processing method. **a** Rapid fabricating method of the pH-responsive helical structure. The helix is polymerized by the rotary holographic ring beam (RHRB) combined with the sample's translation. The circular arrows denote the rotation direction of the RCGH and RHRB, and the straight arrow represents the moving direction of the sample. **b** Generation of the RCGH composed of a CGH and RLPM. **c** Schematic diagram of the holographic femtosecond laser processing system used to fabricate the microhelix. **d** Diagrammatic sketch of the expansion and contraction of the pH-triggered hydrogel-based helix. **e** Shrinking/swelling mechanism of the pH-responsive hydrogel. The upper row shows the schematic mechanism of the expansion and contraction of pH-responsive hydrogels. The bottom row denotes the SEM images of the hydrogel porosities in the contracted (left) and expanded (right) states. Scale bar: 500 nm. **f** Schematic diagrams of various microorganisms in nature and optical images of the corresponding biomimetic microhelices fabricated using the RHRB in one step. Scale bar: 25 μm.

beams with specific intensity distributions, while the BG is crucial for separating the generated Bessel beams from the zero-order light, which originates from the pixelation effect of the SLM[43]. Therefore, the final phase distribution of the CGH can be expressed as

$$Ph_1(x_0, y_0) = mod\left(n\alpha + \frac{2\pi r}{r_0} + \frac{2\pi x_0}{d}, 2\pi\right) \quad (1)$$

where x_0 and y_0 are the horizontal and vertical coordinates on the SLM plate, n is the topological charge of the SPP, $\alpha = tan^{-1}(y_0/x_0)$, $r = \sqrt{x_0^2 + y_0^2}$, r_0 denotes the radius of the axicon, and d is the period of the BG. The single laser point was changed into a Bessel ring beam after modulation by the CGH.

To generate RLPM, we superimposed multiple local phase modulations (LPMs) with an increased oblique angle (θ_t) in a time sequence using commercial software (GIF Movie Gear) at 20 frames (Supplementary Fig. S1). The LPM was a half-and-half energy-regulated element, where the black area denotes the zero phase with zero energy after

regulation, and the white area represents the original phase with unaltered energy[44,45]. The Bessel ring beam was changed into a half-ring beam after modulation by this LPM. The time-dependent θ_t can be determined by time (t) and the rotating angle (θ_0), which is expressed as

$$\theta_t = 20t\theta_0 \tag{2}$$

Finally, by adding RLPM to the CGH, the RCGH was synthesized with the following phase distribution:

$$Ph(x_0, y_0, t) = \begin{cases} mod\left(n\alpha + \frac{2\pi r}{r_0} + \frac{2\pi x_0}{d}, 2\pi\right), & y_0 cos(\theta_t) > x_0 sin(\theta_t) \\ 0, & else \end{cases} \tag{3}$$

After modulation by the RCGH, the half-ring beam could become a rotary holographic ring beam (RHRB), as shown in the middle diagram of Fig. 1a.

To fabricate the microhelical structure, a drop of the pH-responsive hydrogel was added to a cover glass that was fixed on a piezoelectric platform (Fig. 1c). Once the RHRB was focused into the hydrogel by an oil immersion lens (60×, NA=1.35), the piezoelectric platform began to simultaneously scan along a straight line in the Z-direction. The rotating ring beam combined with the linear movement of the platform rapidly generated a microhelix, as shown in the right diagram of Fig. 1a. Owing to the fast linear movement of the platform and the rapid rotation of the RCGH, a microhelix could be formed in less than 1 s (Supplementary Movie S1), which is almost 100 times faster than the direct laser writing of microhelices. To demonstrate the high efficiency of our processing strategy, a large array of a thousand hydrogel microhelices was fabricated within 0.5 h, which consisted of the fabrication and mechanical movement times of the sample platform (Supplementary Fig. S2).

The pH-triggered hydrogel was a homemade hydrogel with a pH threshold value of approximately 9 in aqueous solution. Fig. 1d schematically illustrates the response behavior of the hydrogel microhelix, which swelled when the pH exceeded 9 and shrunk when the pH was lower than 9. The 3D morphologies of the microhelices before and after swelling are shown in Supplementary Fig. S3. Our stimuli-responsive hydrogel was a polyacrylic acid (pAAc)-based hydrogel with a mass of terminal carboxyl after polymerization. The swelling and shrinkage mechanisms of the hydrogels are shown in Fig. 1e. When the pH of the solution exceeded 9, the carboxyl lost hydrogen ions and became positively charged. The repulsive forces between the electropositive carboxyls caused the hydrogel to swell. In contrast, when the pH was lower than 9, the electropositive carboxyl combined with a proton and changed into an electroneutral carboxyl[46]. The repulsive force disappeared, and the hydrogel began to collapse. The pH of the solution was adjusted by adding HCl and NaOH solution in turn. To further study the response mechanism of the two-photon polymerized hydrogel, the interior porosities in the contracted and expanded states are shown in Fig. 1e. Obviously, there was an increase in porosity, with the average diameter increasing from 146 (contracted state) to 198 nm (expanded state), which reveals that the expansion of hydrogel is due to water absorption with larger porosity. More details regarding the porosities of the hydrogel are provided in the Experimental section.

The natural world abounds in microorganisms that can serve as templates for developing microhelices with intelligent responses and adaptive locomotion, including spirulina with spiral morphology[47], Escherichia coli with a head and two helical tails[48], sperm with a head and one helical tail[49], and Trypanosoma brucei with a taper-screwed body (Fig. 1f)[50]. These microorganisms can adjust their morphologies and locomotion modes to adapt to the external environment. To prove the universality of our rotary holographic processing method, we fabricated polymorphic biomimetic microhelices in an easy and rapid (<1 s) one-step process. These microhelices can mimic natural microorganisms with shape morphing and adaptive locomotion capabilities. The details of the fabrication process are shown in Supplementary Fig. S4.

Microhelices with designed morphologies controlled by the RHRB

To demonstrate the flexibility and designability of our strategy, microhelices with different morphologies involving varying heights (H) and diameters (D) were fabricated. As illustrated in Fig. 2a, the height of the microhelix was controlled by the scanning speed of the piezoelectric platform (V) and rotating angle (θ_0) of the RCGH. Meanwhile, the diameter was regulated by the topological charge (n) of the RCGH. When the topological charge was increased from 5 to 40, the diameter of the RHRB increased correspondingly, similar to the diameter of the microhelix. (Supplementary Fig. S5). Fig. 2b reveals the increase in the diameter of the microhelix from 7 to 15 μm as the topological charge increased from 10 to 30. The pitch number of our microhelix throughout was three, which could be set by rotating the RCGH three times during fabrication.

Fig. 2c, d show that the height of the microhelix was inversely related to the rotation angle and positively correlated with the scanning speed. The rotation angle (θ_0)

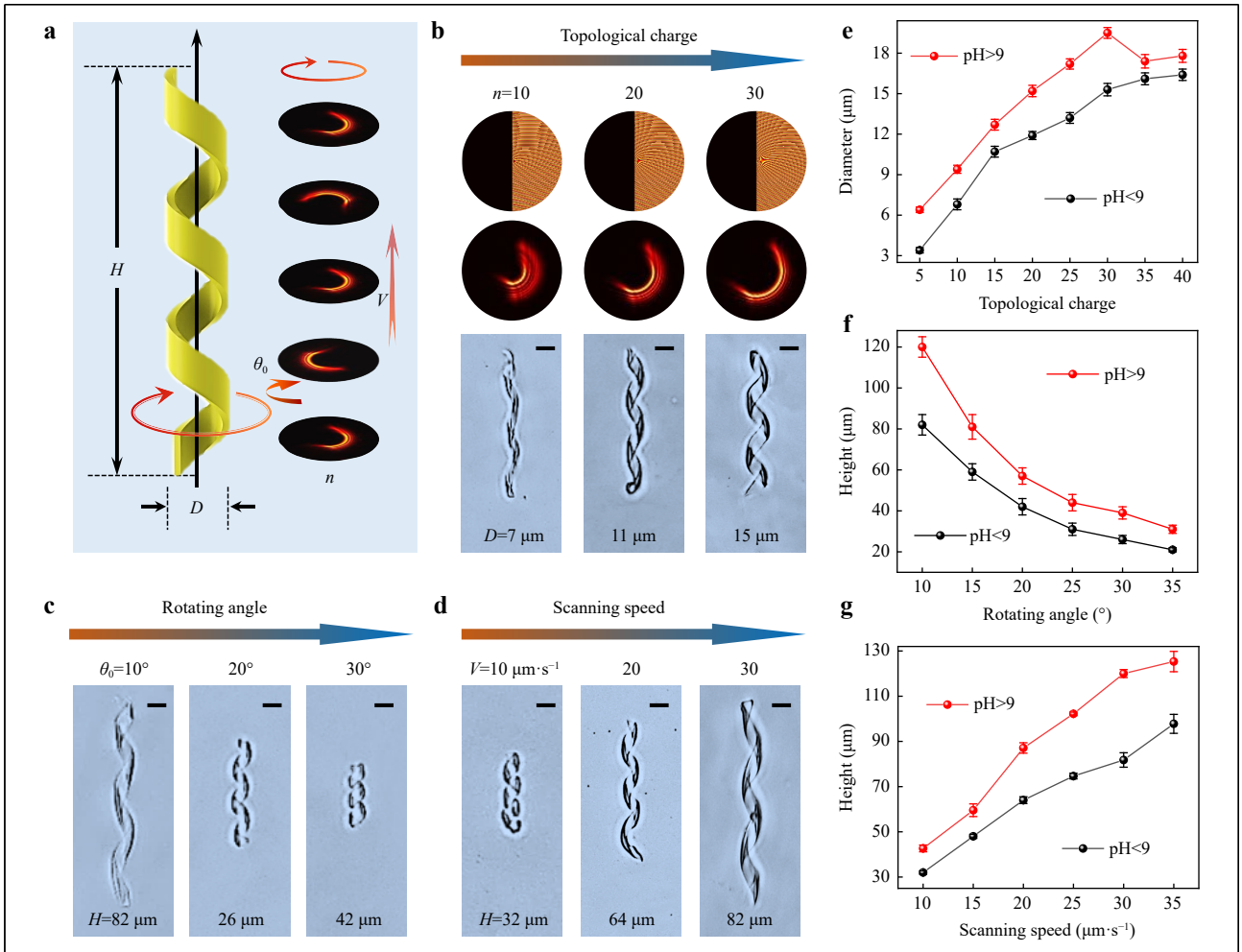

Fig. 2 Microhelices with designed morphologies fabricated using the RHRB. **a** Diameter D of the microhelix depending on the topological charge n of the RHRB, and the height of the microhelix H controlled by the scanning speed of the sample platform V and rotation angle θ_0 of the RHRB. **b** Diameter of the microhelix increasing with increasing topological charge. **c** Height of the microhelix decreasing with increasing rotation angle. **d** Height of the microhelix increasing with increasing scanning speed. **e** Effect of topological charge on the diameter of the microhelix in the swelling and shrinking states. **f**,**g** Effects of rotating angle and scanning speed on the height of the microhelix in the swelling and shrinking states. All scale bars: 10 μm.

of the RCGH was the oblique angle difference between the two CGHs of adjacent frames (Supplementary Fig. S1). Obviously, a larger θ_0 meant that the RCGH rotated by a circle (360°) with fewer CGHs and shorter fabrication time owing to the fixed frame number (20 frames) and constant pitch number (3). A shorter fabrication time combined with a constant scanning speed of the sample platform decreased the height of the microhelix. As θ_0 increased from 10° to 30°, the height of the microhelix decreased from 82 to 26 μm (Fig. 2c). In contrast, a larger scanning speed of the sample platform (V) increased the height of the microhelix, as shown in Fig. 2d, where the height increased from 32 to 82 μm with$V$ increasing from 10 to 30 μm s^{-1}.

The microhelices illustrated above were all in a contracted state, and there was a slight difference between the contracted and expanded microhelices. Therefore, we further studied the quantitative relationship between the microhelix sizes (D and H) and the fabrication parameters (n, V, and θ_0) in both the contracted and expanded states. As shown in Fig. 2e, in contrast to the positive relationship between the diameter of the contracted microhelix and the topological charge of the RCGH, the diameter of the expanded microhelix decreased when the topological charge (n) exceeded 30. We assumed that this decrease was due to the large diameter of the microhelix in the expanded state. Therefore, the hydrogel microhelix was too soft to maintain its shape. The detailed morphologies of microhelices with different diameters are shown in Supplementary Fig. S6. The dependence of the heights of the microhelices on the rotating angle (θ_0) and scanning

speed (V) in both the contracted and expanded states is depicted in Figs. 2f, g, where they all demonstrate the same changing trends in the two states. The details of the microhelix morphologies at different heights are shown in Supplementary Figs. S7 with S8.

As a robust microhelix fabrication method, our rotary holographic processing strategy produces microhelices with diverse morphologies. The diameter of the helical microrobot ranged from 7 to 21 μm. The maximum height of the microrobot was determined by the maximum stroke of the piezoelectric platform, which was 200 μm, whereas the minimum height of the helical microrobot (pitch number=3) with clear spiral morphology was 26 μm. In addition to the diameter and height, the pitch number and helical sense of the microhelix could also be easily controlled (Supplementary Fig. S9). Moreover, although the hydrogel-based helical microrobots are prone to deform owing to the small modulus of the hydrogel, our helical microrobot fabricated using the RHRB exhibited excellent morphological and actuation stability.

Adaptive locomotion of shape-morphing helical microswimmers under a constant rotating magnetic field

The polymerized microhelices were immersed in a magnetic Fe_3O_4 nanoparticle (NP, 160 nm) solution (5 mg mL^{-1}) for 24 h to gain magnetism and become microswimmers (Fig. 3a). The Fe_3O_4 NPs were covered with a nanolayer of SiO_2, which acted as a protective layer to prevent Fe_3O_4 from reacting with the HCl and NaOH solutions (Supplementary Movie S2). Furthermore, hydroxide radicals were modified on the surface of SiO_2 to help the Fe_3O_4 NPs distribute uniformly in deionized (DI) water and attach to the hydrogel microhelix. To characterize the magnetization of the Fe_3O_4 NPs and magnetic microswimmers, a vibrating sample magnetometer (VSM) was used, with the VSM loops illustrated in Fig. 3b, which reveals the soft magnetic behavior of the Fe_3O_4 NPs and magnetic microswimmers.

The helical microswimmers could be actuated under a rotating magnetic field generated by a homemade triaxial Helmholtz coil system (Supplementary Fig. S10). We first explored the magnetic actuation properties of our shape-morphing helical microswimmer in the contracted and expanded states (Supplementary Note S1 and Fig. S11). Interestingly, a microswimmer demonstrated two different swimming modes in the contracted and expanded states. Specifically, the helical microswimmer performed a tumbling motion in the contracted state and a corkscrewing motion in the expanded state under a constant rotating magnetic field (CRMF), as shown in Fig. 3c and Supplementary Movie S3. The precession angle (β, the angle between the field rotation axis and the helical axis) was 90° for the tumbling motion and 0° for the corkscrewing motion. It is worth noting that the locomotion transition merely relied on the shape morphing of the microswimmer in response to the solution pH value change, rather than on altering the external magnetic field. The helical microswimmer was actuated using a magnetic field with a frequency of 5 Hz and a magnetic strength of 15 mT.

To explain the locomotion transition of the microswimmer, a simplified theoretical model was established, as shown in Supplementary Note S2 and Fig. S12. It has been previously reported that magnetically actuated helical microswimmers exhibit a transition from tumbling to corkscrewing with an increase in the magnetic field frequency[51,52]. Tumbling occurs at a low frequency with a precession angle of 90°, while corkscrewing appears at a high frequency with the precession angle gradually diminishing as the field frequency increases. The frequency separating tumbling and corkscrewing is known as the transition frequency (w_t), which is a function of the external magnetic field and the body geometry and magnetization orientation of the helical microswimmer[53]. According to this simplified theoretical model, we can derive the transition frequency (w_t) formulas, where it can be concluded that the diameter (D) is the most important parameter that affects the transition frequency. Clearly, w_t decreases as the diameter increases. Therefore, a contracted microswimmer with a small diameter exhibits a tumbling motion, whereas an expanded microswimmer with a large diameter exhibits a corkscrewing motion because the actuation frequency is less than w_t of the contracted microswimmer but greater than w_t of the expanded microswimmer.

Having understood the mechanism of the locomotion transition of the microswimmer, we attempted to separately analyze the swimming characteristics of microswimmers in the contracted and expanded states. To gain deeper insight into the tumbling motion of contracted helical microswimmers, we investigated the detailed locomotion process (Fig. 3d) and mechanism (Supplementary Fig. S13). The schematic diagram and time-lapse image in Fig. 3d show that the microswimmer tumbled forward along its short axis. In addition, a simplified model was established to explain the locomotion mechanism of microswimmer tumbling. The forces exerted on the microswimmer at a certain moment are shown in Supplementary Fig. S13. The tumbling motion can be considered an equilibrium between the magnetic driving torque and drag torque. The drag force originates from the

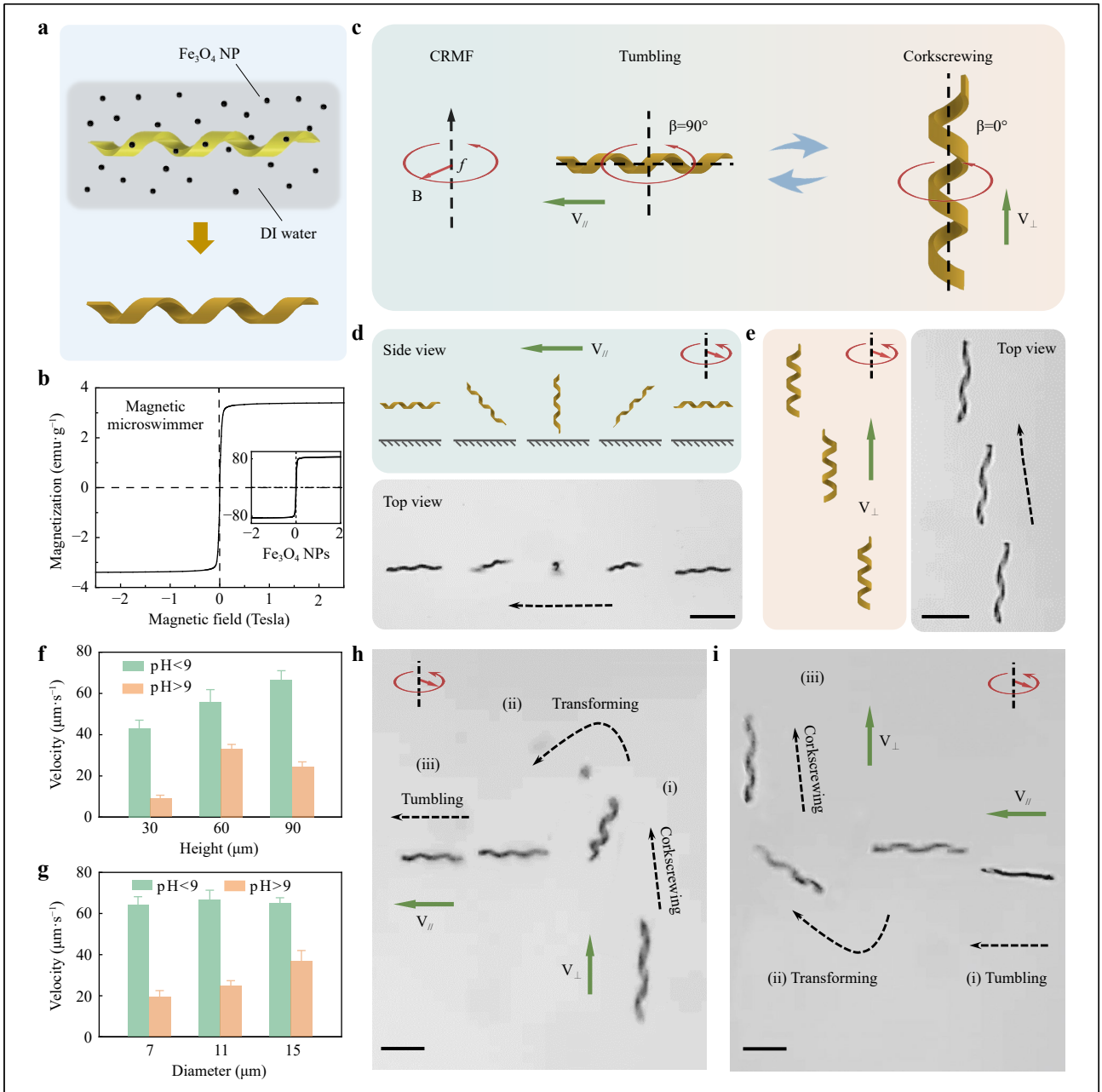

Fig. 3 Adaptive locomotion of shape-morphing helical microswimmers under a constant rotating magnetic field. **a** Printed hydrogel microswimmer immersed in Fe_3O_4 nanoparticle suspension, gaining magnetism for the actuation test. **b** Mass magnetization curve of the magnetic microswimmer and Fe_3O_4 nanoparticles measured using a vibrating sample magnetometer (VSM). **c** Schematics of magnetic actuation for the pH-responsive helical microswimmer in the contracted and expanded states. The contracted microswimmer exhibits tumbling motion with the rotation axis perpendicular to the helical axis, whereas the expanded microswimmer demonstrates corkscrewing motion with the rotation axis along the helical axis. The magnetic field is a constant rotating magnetic field (CRMF) with a strength of 15 mT and a frequency of 5 Hz. **d** Schematics and time-lapse image of the tumbling motion of the contracted helical microswimmer, where $V_{//}$ indicates that V is parallel to B. **e** Schematics and time-lapse image of the corkscrewing motion of the expanded helical microswimmer, where $V_\perp$ indicates that V is perpendicular to B. **f**, **g** Velocities of the contracted and expanded microswimmers with different heights and diameters. **h** Dynamic transition process of the microswimmer from tumbling to corkscrewing. The transition is realized by changing the pH value during the actuation of the microswimmer. **i** Reverse process compared with **h**, from corkscrewing to tumbling, owing to the increasing pH value. Scale bar: 50 μm.

hydrodynamic interaction between the microswimmer and the boundary[54,55]. Owing to the distinct boundary conditions, there was a velocity difference between the two ends of the microswimmer, which caused non-coincidence

of the mass and rotation centers. Therefore, the contracted microswimmer could move forward. Further details are provided in Supplementary Note S3. By contrast, the expanded helical microswimmer was corkscrewed forward, as shown in Fig. 3e. This corkscrewing motion is consistent with the motion of current helical microswimmers, which can be explained by magnetic helical micromotor propulsion theory[56]. Additionally, experiments to investigate the precise steering of the microswimmers are shown in Supplementary Fig. S14.

There were three major differences between the tumbling and corkscrewing behaviors of our microswimmer: locomotion mode, motion direction, and swimming velocity. First, the locomotion modes tumbled when contracted and corkscrewed when expanded. Second, the contracted microswimmer tumbled forward with a velocity ($V_{//}$) parallel to the magnetic field plane, whereas the expanded microswimmer corresponded to a velocity ($V_{\perp}$) vertical to the magnetic field plane. Therefore, the directions of tumbling and corkscrewing were almost perpendicular (Fig. 3c). Third, the swimming velocities of the microswimmers in the contracted and expanded states were quantitatively studied, as illustrated in Fig. 3f, g. We concluded that the tumbling velocities were approximately one–four times larger than the corkscrewing velocities (Supplementary Table S1). More specifically, the tumbling velocity is positively related to the height of the microswimmer and has little relation with the diameter of the microswimmer. The corkscrewing velocity first increases and then decreases with an increase in the microswimmer height and is positively related to the microswimmer diameter. Given the significant velocity difference and steerability of the microswimmer before and after the expansion, we chose the microswimmer with a height of 90 μm and a diameter of 11 μm for the remaining experiments.

After studying and comparing the magnetic actuation properties of microswimmers in the expanded and contracted states, we focused on the dynamic transition process between tumbling and corkscrewing motions, which can be realized by changing the pH value during the motion of the microswimmer. For example, the microswimmer initially expanded and corkscrewed forward (Fig. 3h(i)). The pH of the solution was lower than 9 when HCl solvents were added, followed by shrinkage and transformation of the microswimmer from corkscrewing to tumbling (Fig. 3h(ii)). Finally, the contracted microswimmer tumbled away (Fig. 3h(iii)). In contrast, as illustrated in Fig. 3i, the tumbling-to-corkscrew dynamic transition was realized by altering the solution pH to exceed 9 when actuating the microswimmer. The details of the dynamic transition are shown in Supplementary Movie S4. The dynamic transition of a microswimmer's locomotion mode relies only on the shape morphing of the microswimmer instead of on the changing of the external magnetic field.

Demonstrations of traversing complex terrains and targeted drug delivery based on the tumbling-to-corkscrewing transition of helical microswimmers

In vivo environments are extremely complex owing to their various biochemistry ingredients and biological obstacles such as folds and cells on the vascular surface, which are primarily within the range of 1–100 μm. Therefore, it is essential to explore smart microrobots that can sense biochemical signal changes and adapt their shapes and locomotion mechanisms to swim across biological obstacles and reach the target position. As a proof-of-concept, we investigated the propulsion and navigation of our helical microswimmer in an in vitro simulation of the biological environment, which could provide admirable technical tools for biomedical applications.

First, we explored the capability of our morphable microswimmer to traverse microscale 3D terrains based on the tumbling-to-corkscrewing transition under a CRMF. A microwall with a width of 10 μm and a height of 60 μm was constructed via fs-DLW (Supplementary Fig. S15a). When the helical microswimmer was in a contracted state and tumbled forward under the rotating magnetic field, it could easily stride over the wall without hindrance (Supplementary Movie S5). However, the expanded helical microswimmer with the corkscrewing motion was blocked by the microwall (Supplementary Fig. S16). Although this expanded microswimmer can swim across the microwall in a corkscrewing motion by precisely adjusting the direction of the external magnetic field, the operational process is complex and time-consuming[57].

An integrated microchannel with microwalls and a microtunnel was designed to better simulate the complex 3D terrains of an in vivo biological environment (Fig. 4a and Supplementary Fig. S15b). Three walls with a width of 10 μm and a height of 60 μm were fabricated to form two microchannels. As shown in Fig. 4b, the contracted microswimmer was initially in Channel I, followed by rapid tumbling across the middle wall, which could not be realized by the expanded microswimmer. After entering Channel II, the microswimmer began to swell because of the pH change. Fig. 4c shows that the expanded microswimmer could corkscrew through the microtunnel, which could not be accomplished by the contracted microswimmer. Here, the microtunnel was 60 μm in height

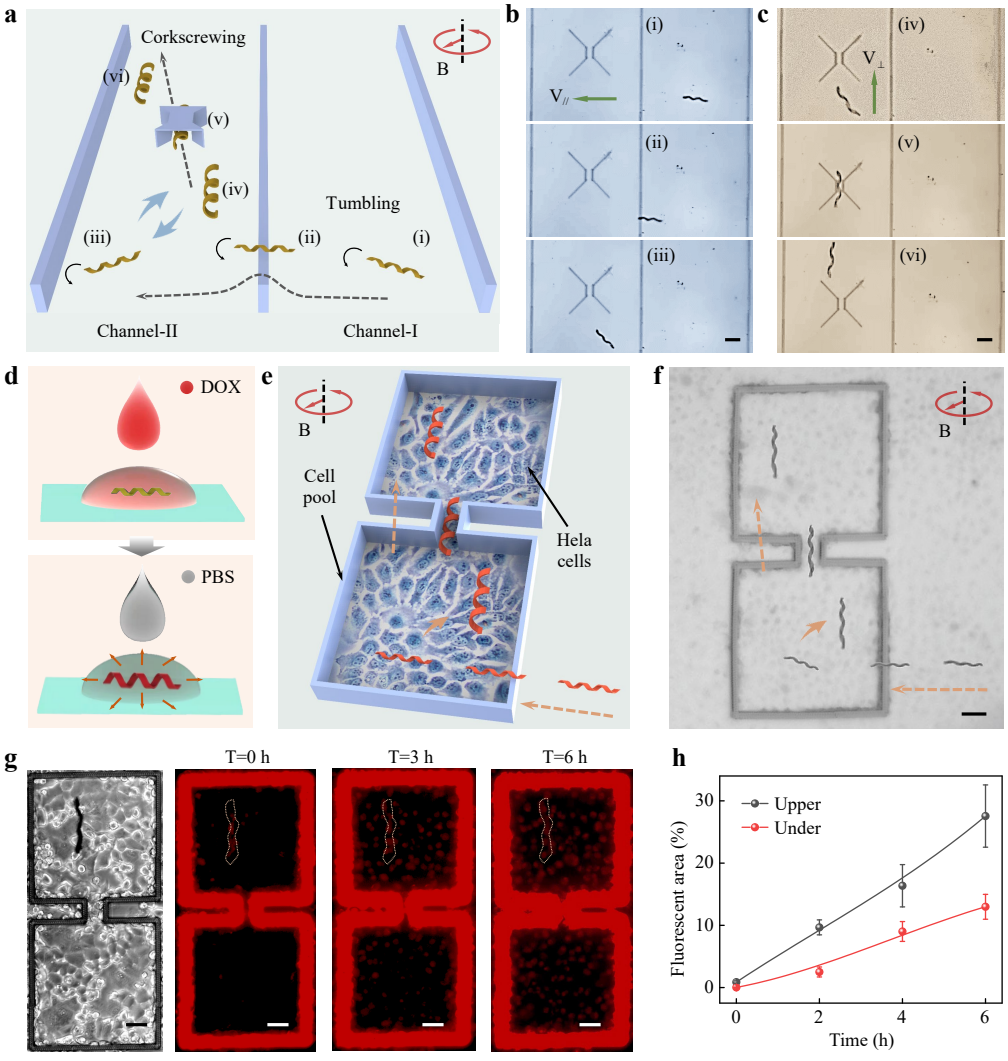

Fig. 4 Demonstrations of traversing complex terrains and targeted drugs delivery based on the tumbling-to-corkscrewing transition of helical microswimmers. **a** Schematics of the microswimmer traversing complex terrains. The contracted helical microswimmer tumbles across the microwall, and the expanded helical microswimmer corkscrews through the microtunnel. The entire process is actuated by a CRMF. Time-lapse images of the tumbling across the microwall **b** and corkscrewing through the microtunnel **c**. **d** Hydrogel helical microswimmer absorbing a drug in high-concentration DOX solution and spreading drugs in PBS. **e** Schematics of the microswimmer achieving targeted drug delivery in complex terrains. The contracted helical microswimmer with drugs tumbles into the Hela cell micropool, whereas the expanded helical microswimmer corkscrews through the microchannel and reaches the target position to release the drugs. **f** Optical image of targeted drug delivery corresponding to **e**. **g** Optical image of microswimmer with drugs at the target position, and time-lapse images of the red DOX fluorescence diffusion process. **h** Quantitative statistics of the DOXs diffusing in the upper micropool (with the microswimmer) and lower micropool (without the microswimmer). Scale bar: 50 μm.

with a central tunnel width of 25 μm, which was slightly wider than the diameter of the expanded microswimmer. Details of the process of traversing the integrated microchannel are shown in Supplementary Movie S6.

Then, we explored the applications of morphable microswimmers in targeted cargo (microparticles or drugs) delivery where microswimmers traverse complex terrains based on the tumbling-to-corkscrewing transition. The targeted microparticle (MP) delivery is shown in Supplementary Fig. S17, in which an SiO_2 MP with the diameter of 20 μm was directly transported and released. The details of this process are shown in Supplementary Movie S7. Moreover, the hydrogel microswimmer with internal nanopores (Fig. 1f) could carry and release drugs at the targeted position. As shown in Fig. 4d, the hydrogel microswimmer was initially immersed in a DOX solution (1 mg ml^{-1}) for 0.5 h, during which the microswimmer was in contracted state and absorbed DOXs. The

microswimmer loaded with DOXs was then transferred to phosphate buffered saline (PBS), where the microswimmer start to swell and releases the drugs. The releasing is realized by the diffusion of DOXs from the nanopores of hydrogel microswimmer. Our earlier study found that this pH-responsive hydrogel can swell in PBS (pH~7.4) without deliberately changing the constituents of hydrogel. We assumed that this is due to the HPQ_4^{2-} and $H_2PQ_4^-$ in the PBS partially breaking the hydrogen bonds between PAAc and PNIPAAm, and causing the deprotonation of carboxyl groups, which was experimentally validated[39]. This result makes sure that our hydrogel microswimmers have the potential in biological applications.

On the basis of the tumbling-to-corkscrewing transition and drug diffusion of the hydrogel microswimmer, targeted drug delivery by crossing complex terrains was realized (Fig. 4e). The terrain consisted of a cell micropool fabricated using fs-DLW with HeLa cells cultured inside. The micropool, bound by a microwall with a height of 60 μm and a width of 10 μm, consisted of two square pools connected by a microchannel (Supplementary Fig. S15c). HeLa cells are a type of tumor cell that can maintain good biological viability in solution with a pH value of approximately 7 and have been extensively studied for cell therapy[58,59]. Initially, HeLa cells were cultured in a micropool with a pH value of less than 7. Drug-loaded helical microswimmers were transferred to the surroundings of the micropool. Once a magnetic field was applied, the contracted microswimmer tumbled across the wall and entered the lower cell pool. Then, the microswimmer started to swell after adding the PBS solution to adjust the pH value back to ~7.4. The expanded microswimmer corkscrews forward to pass through the microchannel (width ~50 μm), and finally arrives at the upper cell pool (Fig. 4f).

After reaching the target position, DOXs loaded in the expanded microswimmer started to spread and entered the HeLa cells in the vicinity. The optical and fluorescence images demonstrating the diffusion process are shown in Fig. 4g. After six hours of diffusion, HeLa cells in the upper micropool showed larger areas of red fluorescence than those in the lower micropool. Quantitative studies on the comparison of red fluorescence intensity in the upper and lower cell pools were carried out, and the results are shown in Fig. 4h. Statistics indicate that the DOXs were delivered to the targeted position, and there was no visible DOX diffusion along the swimming path. To eliminate the effect of the hydrogel itself on the distribution of red fluorescence, we conducted a control experiment by magnetically actuating the microswimmer without loaded DOXs and found that there was no red fluorescence in the upper and lower cell pools (Supplementary Fig. S18).

Our proposed strategy for fabricating shape-morphing helical microswimmers at the microscale is essential for accurate therapy of cells, tissues, and capillaries. This may confuse researchers because of biomedical applications that exploit the pH value change in the internal environment. Indeed, the critical pH value of our hydrogel was approximately 9 in a strong alkali solution, whereas it decreased to approximately 7.4 in PBS. Therefore, the microswimmer will tumble (contract) in solution at pH<7 and corkscrew (expand) at pH~7.4, which is suitable for biological applications because the pH of normal and tumor environments are 7.4 and <7[60,61], respectively. Moreover, the targeted drug delivery shown above is merely focused on drug diffusion rather than HeLa cell killing, which is a proof-of-concept demonstration and still has greater room for improvement. Further efforts can be made to compound light- or heat-triggered hydrogels that are more biofriendly and degradable. Helical microswimmers with adaptive locomotion based on these hydrogels are expected to promote the progression of microswimmers in future clinical applications.

In summary, a rotary holographic processing method is proposed to fabricate reconfigurable helical microswimmers at the microscale (1–100 μm) with controllable sizes and diverse morphologies easily and efficiently (<1 s), which is approximately 100 times faster than direct laser writing. A helical microswimmer with pH-triggered hydrogel as its base soft matrix and Fe_3O_4 NPs as the actuation material is capable of shape morphing when the pH value of the solution changes. Interestingly, reconfigurable helical microswimmers demonstrate adaptive locomotion under a constant rotating magnetic field, that is, tumbling when shrinking and corkscrewing when swelling. Based on this tumbling-to-corkscrewing transition, an in vitro simulation of the biological environment was conducted by propelling a morphable microswimmer to traverse complex terrains, including microwalls and integrated microchannels. As a proof of concept, we explored the applications of our helical microswimmers in targeted drug (DOXs) delivery to treat HeLa cells after navigating complex terrains, hence validating the application of the reconfigurable microswimmer in accurate treatment and targeted cell therapy.

Materials and Methods

Holographic femtosecond laser processing system

The system was constructed by integrating spatial light modulation modules into a femtosecond laser direct-writing system. The femtosecond laser was produced using

a Ti:sapphire laser oscillator (Chameleon vision-S, Coherent Corp.) with a central wavelength of 780 nm, a repetition rate of 80 MHz, and a pulse duration of 75 fs. After reflection from the liquid-crystal SLM loaded with the CGH (1920 × 1 080 pixels, 256 gray levels, a pixel pitch of 8 μm, Pluto NIR II, Holoeye), the Gaussian beam was modulated into a Bessel beam. The Bessel beam was focused into the pH-responsive hydrogel using an oil objective lens (60×, NA=1.35, Olympus). The hydrogel was dropped onto a commercial glass, which was fixed on a 3D nanopositioning stage (E545, Physik Instrumente). By driving the stage along a preprogrammed path while displaying the RHRB, a hydrogel helical microswimmer was printed with high efficiency.

Preparation of the pH-responsive hydrogel

The pH-responsive hydrogel comprised two major components. Component 1 was obtained by adding 0.8 mL AAc (99%), 1.6 g N-isopropylacrylamide (98%), and 0.15 g polyvinylpyrrolidone (Mw~130000) to 1 mL ethyl lactate (98%), followed by ultrasonic mixing for 10 min. Component 2 was obtained by adding 100 μL 4,4′bis(diethylamino) benzophenone into 500 μL N, N-dimethylformamide, followed by ultrasonic mixing for 10 min. The final hydrogel was synthesized by mixing 2.5 mL of Component 1, 600 μL of Component 2, 0.5 mL dipentaerythritol pentaacrylate (98%), and 0.5 mL triethanolamine (99%) together, followed by 12 h of stirring. The hydrogel had to be stored under yellow light to avoid unnecessary light exposure.

Characterization of the internal nanopore of the hydrogel

The hydrogel microstructures fabricated using femtosecond Bessel beams were immersed in aqueous ammonia (pH > 9) and hydrochloric acid (pH < 9) solutions. After 12 h of freezing in a refrigerator (−80 ℃), the hydrogel microstructures were transferred into a freezer dryer to obtain the freeze-dried contracted and expanded microstructures. The microstructures were then cut using a focused ion beam (FIB) to obtain the internal nanopore morphology, which was photographed using a field-emission scanning electron microscope (SEM).

Preparation of DOX solution

Hydrophilic DOX was purchased from Sigma-Aldrich. The DOX solution was prepared by adding 1 mg DOXs to 1 mL DI water, followed by ultrasonic mixing for 10 min. After polymerization, the hydrogel microswimmers were developed using isopropyl alcohol for 0.5 h. Next, the microswimmers were treated with UV sterilization for 0.5 h and washed using DI water and PBS solution successively. The microswimmers were then soaked in the DOX solution for 0.5 h to absorb the drugs. Finally, the microswimmers were washed with DI water three times to remove the DOXs from the solution rather than from the microswimmer.

Cell culture in the cell micropool

The cell micropool was fabricated via fs-DLW and developed using n-propyl alcohol for 0.5 h. To reduce the fluorescence intensity of the cell micropool, the sample was illuminated with ultraviolet light for 48 h to quench fluorescence. The cell micropool was treated by UV sterilization for 0.5 h and soaked in DI water for 0.5 h and PBS solution for 0.5 h successively. HeLa cells were seeded in the cell micropool and cultured in the cell medium for 48 h, followed by subsequent operations as described above. The HeLa-EGFP cells were obtained from the American Type Culture Collection and cultured in a humidified atmosphere at 37 ℃ with 5% CO_2. The cells were cultured in minimum essential medium supplemented with 1% penicillin/streptomycin and 10% fetal bovine serum (all purchased from Procell Life Science&Technology Co., Ltd.).

Analysis on the fluorescent area

Fluorescent images of the cells were imported into the ImageJ software to analyze the fluorescent area. By setting a threshold of 35–255, the red areas in the RED channel of the image could be identified. The rate of the fluorescent area was determined by dividing the total area of the image by the red areas.

Acknowledgements

This research was supported by the Major Scientific and Technological Projects in Anhui Province (202103a05020005), National Natural Science Foundation of China (Nos. 52075516, 61927814, and 52122511), National Key Research and Development Program of China (No. 2021YFF0502700), Major Scientific and Technological Projects in Anhui Province (201903a05020005), China Postdoctoral Science Foundation (2023M733381 and 2021M703120), USTC Research Funds of the Double First-Class Initiative (YD2340002009), the Joint Fund for New Medicine of USTC (YD2090002016), and the CAS Project for Young Scientists in Basic Research (No. YSBR-049). L.Z. would like to thank the Hong Kong Research Grant Council for support with Project No. JLFS/E-402/18, and the Croucher Foundation Grant with Ref. No. CAS20403. We thank the Experimental Center of Engineering and Material Sciences at USTC for the fabrication and measurement of the samples. This study was partially conducted at the USTC Center for Micro and Nanoscale Research and Fabrication.

Author contributions

R.L. and Y.T. contributed equally to this study. R.L., J.W.L., and D.W. designed the experiments. D.D.J. prepared the pH-responsive materials. R.L., Y.T., and M.D.J. fabricated the samples. R.L. and G.L.L. performed freeze-drying experiments. R.L., C.X., L.R.Z., and S.Y.F. conducted the cell

capture experiments. R.L., Y.T., and Q.Q.Z. analyzed the data and prepared the manuscript. Y.L.H., W.D., J.W.L., L.Z., and J.R.C reviewed and revised the manuscript.

Conflict of interest

The authors declare no competing interests.

Supplementary information is available for this paper at https://doi.org/10.37188/lam.2023.029.

Received: 11 April 2023 Revised: 13 August 2023 Accepted: 24 August 2023
Accepted article preview online: 26 August 2023
Published online: 30 October 2023

References

1. Lauga, E. Bacterial hydrodynamics. *Annual Review of Fluid Mechanics* **48**, 105-130 (2016).
2. Malo, A. F. et al. Sperm design and sperm function. *Biology Letters* **2**, 246-249 (2006).
3. Spagnolie, S. E. & Lauga, E. Comparative hydrodynamics of bacterial polymorphism. *Physical Review Letters* **106**, 058103 (2011).
4. Medina-Sánchez, M. et al. Swimming microrobots: soft, reconfigurable, and smart. *Advanced Functional Materials* **28**, 1707228 (2018).
5. Yang, T. et al. Reconfigurable microbots folded from simple colloidal chains. *Proceedings of the National Academy of Sciences of the United States of America* **117**, 18186-18193 (2020).
6. Breger, J. C. et al. Self-folding thermo-magnetically responsive soft microgrippers. *ACS Applied Materials & Interfaces* **7**, 3398-3405 (2015).
7. Jin, Q. R. et al. Untethered single cell grippers for active biopsy. *Nano Letters* **20**, 5383-5390 (2020).
8. Zhang, J. C. et al. Liquid crystal elastomer-based magnetic composite films for reconfigurable shape-morphing soft miniature machines. *Advanced Materials* **33**, 2006191 (2021).
9. Zeng, H. et al. Light-fueled microscopic walkers. *Advanced Materials* **27**, 3883-3887 (2015).
10. Palagi, S. et al. Structured light enables biomimetic swimming and versatile locomotion of photoresponsive soft microrobots. *Nature Materials* **15**, 647-653 (2016).
11. Rogóż, M. et al. Light-driven soft robot mimics caterpillar locomotion in natural scale. *Advanced Optical Materials* **4**, 1689-1694 (2016).
12. Ghosh, A. et al. Gastrointestinal-resident, shape-changing microdevices extend drug release in vivo. *Science Advances* **6**, eabb4133 (2020).
13. Hu, W. Q. et al. Small-scale soft-bodied robot with multimodal locomotion. *Nature* **554**, 81-85 (2018).
14. Kim, Y. et al. Printing ferromagnetic domains for untethered fast-transforming soft materials. *Nature* **558**, 274-279 (2018).
15. Huang, G. Y. et al. Magnetically actuated droplet manipulation and its potential biomedical applications. *ACS Applied Materials & Interfaces* **9**, 1155-1166 (2017).
16. Dong, Y. et al. Magnetic helical micro-/nanomachines: recent progress and perspective. *Matter* **5**, 77-109 (2022).
17. Peyer, K. E. , Zhang, L. & Nelson, B. J. . Bio-inspired magnetic swimming microrobots for biomedical applications. *Nanoscale* **5**, 1259-1272 (2013).
18. Huang, H. W. et al. Soft micromachines with programmable motility and morphology. *Nature Communications* **7**, 12263 (2016).
19. Yoshida, K. & Onoe, H. Soft spiral-shaped microswimmers for autonomous swimming control by detecting surrounding environments. *Advanced Intelligent Systems* **2**, 2000095 (2020).
20. Badami, A. S. et al. Effect of fiber diameter on spreading, proliferation, and differentiation of osteoblastic cells on electrospun poly (lactic acid) substrates. *Biomaterials* **27**, 596-606 (2006).
21. Liu, Z. W. , Chen, W. & Papadopoulos, K. D. Bacterial motility, collisions, and aggregation in a 3-μm-diameter capillary. *Biotechnology and Bioengineering* **53**, 238-241 (1997).
22. Tan, Y. L. et al. Bioinspired multiscale wrinkling patterns on curved substrates: an overview. *Nano-Micro Letters* **12**, 101 (2020).
23. Zhang, L. et al. Artificial bacterial flagella: fabrication and magnetic control. *Applied Physics Letter* **94**, 064107 (2009).
24. Zhang, L. et al. Characterizing the swimming properties of artificial bacterial flagella. *Nano Letters* **9**, 3663-3667 (2009).
25. Ghosh, A. & Fischer, P. Controlled propulsion of artificial magnetic nanostructured propellers. *Nano Letters* **9**, 2243-2245 (2009).
26. Gao, W. et al. Bioinspired helical microswimmers based on vascular plants. *Nano Letters* **14**, 305-310 (2014).
27. Kawata, S. et al. Finer features for functional microdevices. *Nature* **412**, 697-698 (2001).
28. Zhang, Y. L. et al. Designable 3D nanofabrication by femtosecond laser direct writing. *Nano Today* **5**, 435-448 (2010).
29. Ceylan, H. *et al.* 3D printed personalized magnetic micromachines from patient blood–derived biomaterials. *Science Advances* **7**, eabh0273 (2021).
30. Bozuyuk, U. et al. Light-triggered drug release from 3D-printed magnetic chitosan microswimmers. *ACS Nano* **12**, 9617-9625 (2018).
31. Ceylan, H. et al. 3D-printed biodegradable microswimmer for theranostic cargo delivery and release. *ACS Nano* **13**, 3353-3362 (2019).
32. Lee, Y. W. et al. 3D-printed multi-stimuli-responsive mobile micromachines. *ACS Applied Materials & Interfaces* **13**, 12759-12766 (2021).
33. Tottori, S. et al. Magnetic helical micromachines: fabrication, controlled swimming, and cargo transport. *Advanced Materials* **24**, 811-816 (2012).
34. Wang, X. P. et al. 3D printed enzymatically biodegradable soft helical microswimmers. *Advanced Functional Materials* **28**, 1804107 (2018).
35. Peters, C. et al. Degradable magnetic composites for minimally invasive interventions: device fabrication, targeted drug delivery, and cytotoxicity tests. *Advanced Materials* **28**, 533-538 (2016).
36. Qiu, F. M. et al. Noncytotoxic artificial bacterial flagella fabricated from biocompatible ORMOCOMP and iron coating. *Journal of Materials Chemistry B* **2**, 357-362 (2014).
37. Jia, R. et al. Detoxification of deoxynivalenol by *Bacillus subtilis* ASAG 216 and characterization the degradation process. *European Food Research and Technology* **247**, 67-76 (2021).
38. Machen, T. E. & Paradiso, A. M. Regulation of intracellular pH in the stomach. *Annual Review of Physiology* **49**, 19-33 (1987).
39. Xin, C. et al. Environmentally adaptive shape-morphing microrobots for localized cancer cell treatment. *ACS Nano* **15**, 18048-18059 (2021).
40. Xu, B. et al. High efficiency integration of three-dimensional functional microdevices inside a microfluidic chip by using femtosecond laser multifoci parallel microfabrication. *Scientific Reports* **6**, 19989 (2016).
41. Wang, Z. et al. High-throughput microchannel fabrication in fused silica by temporally shaped femtosecond laser bessel-beam-assisted chemical etching. *Optics Letters* **43**, 98-101 (2018).
42. Cai, Z. et al. Dynamic airy imaging through high-efficiency broadband phase microelements by femtosecond laser direct writing. *Photonics Research* **8**, 875-883 (2020).
43. Yang, L. et al. Targeted single-cell therapeutics with magnetic tubular micromotor by one-step exposure of structured femtosecond optical vortices. *Advanced Functional Materials* **29**, 1905745 (2019).
44. Li, R. et al. Stimuli-responsive actuator fabricated by dynamic

asymmetric femtosecond bessel beam for *in situ* particle and cell manipulation. *ACS Nano* **14**, 5233-5242 (2020).
45. Ji, S. Y. et al. High-aspect-ratio microtubes with variable diameter and uniform wall thickness by compressing Bessel hologram phase depth. *Optics Letters* **43**, 3514-3517 (2018).
46. Li, X. et al. Reversible bidirectional bending of hydrogel-based bilayer actuators. *Journal of Materials Chemistry B* **5**, 2804-2812 (2017).
47. Ali, S. K. & Saleh, A. M. Spirulina-an overview. *International Journal of Pharmacy and Pharmaceutical Sciences* **4**, 9-15 (2012).
48. Nataro, J. P. & Kaper, J. B. Diarrheagenic *Escherichia coli*. *Clinical Microbiology Reviews* **11**, 142-201 (1998).
49. Pitnick, S. , Hosken, D. J. & Birkhead, T. R. Sperm morphological diversity. in Sperm Biology (eds Birkhead, T. R. , Hosken, D. J. & Pitnick, S.) (Amsterdam: Elsevier, 2009), 69-149.
50. Matthews, K. R. The developmental cell biology of Trypanosoma brucei. *Journal of Cell Science* **118**, 283-290 (2005).
51. Morozov, K. I. & Leshansky, A. M. Dynamics and polarization of superparamagnetic chiral nanomotors in a rotating magnetic field. *Nanoscale* **6**, 12142-12150 (2014).
52. Leshansky, A. M. , Morozov, K. I. & Rubinstein, B. Y. Shape-controlled anisotropy of superparamagnetic micro-/nanohelices. *Nanoscale* **8**, 14127-14138 (2016).
53. Morozov, K. I. et al. Dynamics of arbitrary shaped propellers driven by a rotating magnetic field. *Physical Review Fluids* **2**, 044202 (2017).
54. Zhang, L. et al. Controlled propulsion and cargo transport of rotating nickel nanowires near a patterned solid surface. *ACS Nano* **4**, 6228-6234 (2010).
55. De Mestre, N. J. & Russel, W. B. Low-reynolds-number translation of a slender cylinder near a plane wall. *Journal of Engineering Mathematics* **9**, 81-91 (1975).
56. Morozov, K. I. , Alexander, M. & Leshansky, A. M. The chiral magnetic nanomotors. *Nanoscale* **6**, 1580-1588 (2014).
57. Alcântara, C. C. J. et al. 3D fabrication of fully iron magnetic microrobots. *Small* **15**, 1805006 (2019).
58. Zhu, J. et al. pH-Controlled delivery of doxorubicin to cancer cells, based on small mesoporous carbon nanospheres. *Small* **8**, 2715-2720 (2012).
59. Zhang, D. et al. Tumor microenvironment activable self-assembled DNA hybrids for pH and redox dual-responsive chemotherapy/PDT treatment of hepatocellular carcinoma. *Advanced Science* **4**, 1600460 (2017).
60. Wang, Y. G. et al. A nanoparticle-based strategy for the imaging of a broad range of tumours by nonlinear amplification of microenvironment signals. *Nature Materials* **13**, 204-212 (2014).
61. Webb, B. A. et al. Dysregulated pH: a perfect storm for cancer progression. *Nature Reviews Cancer* **11**, 671-677 (2011).